Non-Faradaic aptasensor based on NH$_2$-GO/PPy for the detection of 17β-estradiol

Anjam Waheed[1] · Mohd H. Mat Zaid[1,2] · Suhainie Ismail[3] · Afifuddin H. Hussain[4] · M. F. Mohd Razip Wee[1]

Abstract

17ß-Estradiol (E2) is an endocrine-disrupting chemical that has become a matter of concern across the globe for more than a decade due to potential health risks. This study reports facile methods to fabricate label-free aptasensor based on the non-Faradaic impedance mode using amine-functionalized graphene oxide polypyrrole (NH$_2$-GO/PPy)-modified gold interdigitated electrode for direct capacitive detection of 17β-estradiol. The as-prepared NH$_2$-GO/PPy nanocomposites have been successfully characterized by field-emission scanning electron microscopy (FESEM), atomic force microscopy, Fourier transform infrared spectroscopy, and electrochemical impedance spectroscopy. The results show that NH$_2$-GO/PPy/IDE was able to detect E2 binding through aptamer conformational change by simply observing the capacitance change before and after immobilization. In addition, the biosensor showed a dynamic range of detection from 100 nM to 1 pM with a low detection limit of about 0.13 pM. The recoveries result also presented in this paper was validated using HPLC exhibited high sensitivity for bisphenol-A (BPA) detection and was successfully applied to detect E2 in real water samples with good recoveries.

Keywords Aptasensor · 17β-Estradiol · Non-Faradaic · Capacitive detection · Nanomaterial

Introduction

Serious concern has been expressed toward endocrine-disrupting compounds (EDCs) in water over their unforeseen harmful effects on humans and wildlife [1]. In this respect, 17ß- estradiol (E2) that belongs to the group of steroids is one of the potent endocrine-disrupting substances (EDC) that can disturb the main structure and functional reproductive system of organisms by imitating natural estrogen hormone activity [2, 3]. Recently, high-performance liquid chromatography (HPLC) [4] and gas chromatography-mass spectrometry (GC–MS) are two instrumental analysis techniques that have been used currently for the determination of E2 [5]. However, they all necessitate expensive equipment, disposables, reagents, highly qualified personnel, and complicated sample preparation procedures. As alternative, biosensors can effectively overcome the constraints of the conventional E2 analysis technique to meet the demand for on-site environmental monitoring [6, 7].

Many previous studies related to E2-based biosensors have been done with several receptors such as antibodies [8], enzymes [9], and MIP [10]. Among these, aptamers have attracted the interest of researchers to detect E2 using different novel detection schemes, including electrochemical [11], colorimetric assays [12], and fluorescent [13]. Briefly, aptamers are single-strand DNA or RNA oligonucleotides with unique conformations designed in vitro through the SELEX (Systematic Evolution of Ligands by Exponential enrichment) or silico selection [14]. Due to their high specificities and selectivity, several targets, including metal ions, small molecules, proteins, and cells, were successfully bound to a unique three-dimensional structure formed by the aptamers [15]. E2 aptamers also have been derived from long- to short-range length nucleotides with varied specificity and selectivity towards E2, some of which were comparable or even stronger than other bioreceptors [16, 17].

✉ M. F. Mohd Razip Wee
m.farhanulhakim@ukm.edu.my

1 Institute of Microengineering and Nanoelectronics, Research Complex, Universiti Kebangsaan Malaysia, Bangi, Malaysia

2 Department of Chemical Sciences, Faculty of Science and Technology, Universiti Kebangsaan Malaysia, Bangi, Malaysia

3 Department of Chemistry, Faculty of Science, Universiti Putra Malaysia, Seri Kembangan, Malaysia

4 Pusat Pengajian Citra Universiti, Universiti Kebangsaan Malaysia, Bangi, Malaysia

Among biosensors, impedimetric biosensors have recently garnered considerable attention, which can be operated in both Faradaic and non-Faradaic modes [18]. This phenomenon is characterized by a capacitive biosensor system observed at the interface between an electrode and an electrolyte solution. Within this context, the precise determination of electron transfer parameters, notably charge transfer resistance (Rct) and Warburg impedance, poses significant challenges when analyzing Nyquist plots. Furthermore, it is important to highlight that the imaginary component of impedance exhibits an inversely proportional relationship with the electrical double-layer capacitance in non-Faradaic electrochemical systems, thereby resulting in an augmentation of capacitance.

In Faradaic modes, redox-active species are required to perform an impedimetric measurement that typically causes finite diffusion/electron transfer to occur across the metal–solution interface in accordance with the Faraday law principle [19]. In contrast to non-Faradaic measurements, no redox probe solution is required because the charge distribution and change in dielectric permittivity/interfacial capacitance are predominant on the electrode/electrolyte. [20]. Typically, Faradaic path can be represented by the Randles' equivalent circuit (RC circuit), which consists of solution resistance (RS), double-layer capacitance (Cdl), electron transfer resistance (Rct), and Warburg impedance (Zw) where three-electrode setup configuration is permitted [21], while for non-Faradic, the Randles equivalent circuit can be replaced with a series resistive (Rt) and capacitive (Ct) terms in parallel to electrical double-layer properties where a simple two-electrode setup is a minimum requirement to run a measurement. [22]. Due to these features, non-Faradaic is preferred for quantification of biomolecules or cells in a point-of-care platform because of its ease of integration and low cost.

Interdigitated electrode (IDE) has been employed widely based on impedance and capacitive biosensors due to its versatility and accessibility[23]. IDE has usually two electrode with a distance between finger electrodes with a line-width limit of 1–5 mm to reduce electrode polarization effects (typically < 100 nm) [24]. It provides a large sensing surface to improve sensitivity, and their performance can be adjusted by modifying their dimensions [25].

To improve the sensitivity of capacitive sensors, the interdigitated electrode modification should be prioritized. Graphene oxide (GO) and its derivative are promising nanomaterial which have been applied for supercapacitor electrodes due to its excellent biocompatibility, abundant oxygen-containing functional groups, and large active surface area [26]. Moreover, the combination of graphene oxide and conducting polymers (CP) could produce stable current density and current confinement on the electrode surface [27]. Previously, considerable efforts have been made to add a small fraction of GO into CP with the goal to increase the effective permittivity and its capacitive properties [28]. There are three commonly employed CP that has been used for capacitance improvement, namely polypyrrole nanowires (PPy) [20], polyaniline (PANI) [29], and poly(3,4-ethylenedioxythiophene) (PEDOT) [30].

Based from the points mentioned above, we fabricated a sensitive capacitive biosensor aptasensor applying a non-Faradic impedance electrochemical system for specific detection of E2. The proposed measuring principle is based on simple changes in interfacial capacitance resulting from the solid-phase binding of E2 with an aptamer probe immobilized on micro-electrodes IDE modified with NH_2-GO/PPy. The utility of this sensor is examined for E2 quantitative determination in the real water sample.

Experimental

Chemicals and instrumentations

Graphene oxide (GO) was obtained commercially purchased from graphene (Netherland). Pyrrole, ammonium persulfate (APS), ethylenediamine (EDA) were purchased from Sigma-Aldrich (St. Louis, USA). Other chemicals were of analytical grade and were used as received obtained. All aqueous solutions were prepared using 18.2 MΩ cm ultra-pure water (Milli-Q water), commercial thin-film Gold Interdigitated Electrode (5/5 μm) (IDE) from Micrux, Spain. Phosphate buffer solution (PBS) was used as a supporting electrolyte with ionic strength at 150 mM NaCl.

In this study, non-Faradaic impedance spectroscopy (EIS) was conducted within a 1 M phosphate-buffered saline (PBS) solution without the presence of any redox probe. A two-electrode configuration was employed, wherein one of the interdigitated electrodes (IDE) served as the working electrode, while the other functioned as both the reference and counter electrodes. The experimental setup utilized an AUTOLAB potentiostat, specifically the model PGSTAT30, equipped with a Frequency Response Analyzer (FRA) module, and controlled via the NOVA program. A sinusoidal voltage signal of 10 mV amplitude at alternating current (AC) was applied across a frequency range spanning from 0.1 Hz to 1 kHz. Notably, all measurements were taken in triplicate to ensure reproducibility and reliability of the data.

Reagents

17β-Estradiol (E2), 17α-ethinyl estradiol (EE2), estriol (E3), and bisphenol A (BPA) were purchased from Merck (Malaysia). Various concentrations of E2 and other interferences solutions were prepared in 10 mM PBS, pH 7.4, while 76-mer E2 aptamer was selected according to

previous studies [31] as an E2 affinity ligand for dissociation constant of 0.13 mM was synthesized by Microgen Inc. (Seoul South Korea). The sequence of the aptamer is given as follows:

NH$_2$-GCTTCCAGCTTATTGAATTACACGCAGAGG GTAGCGGCTCTGCGCATTCAATTGCTGCGCGCTGAA GCGCGGAAGC.

Amine-GO/polypyrrole (NH$_2$-GO/PPy) preparation

Amine Graphene oxide/polypyrrole (NH$_2$-GO/PPy) was prepared according to Pourbeyram et al., 2018 with modification [27]. Firstly, the GO (1 mg/ml) solution from commercial GO was added dropwisely with ethylenediamine (EDA) under ultrasonication to increase the pH level at 11. After this step, EDC/NHS (1 mM/10 mM) was dropped to activate the carboxylate group of GO and, then, allow it to slowly stir on a hot plate (60 °C) for 30 min. At this stage, sodium peroxy disulfate (APS) was added to the reaction solution for 30 min, followed by 0.5 mL of pyrrole. It was then stored at 4 °C for 24 h. Finally, the black precipitate was washed twice with ethanol and distilled water prior to overnight drying in a vacuum oven at 60 °C. The resulting product was designated as NH$_2$-GO/PPy.

Fabrication of NH$_2$-GO/PPy-modified IDE

As shown in Fig. 1, the aptasensor platform was deposited by a thin solid film of NH$_2$-GO/PPy onto the working area. Then we heated it at 60 °C for two minutes. Prior to drying, the IDE was cleaned with acetone under sonication for 5 min, then rinsed with distilled water, and dried under a nitrogen stream(N$_2$). Then, the prepared electrode was immersed in the glutaraldehyde solution for about 1 h. To remove any unbound aptamers on the surface electrode, the electrode surface was rinsed with phosphate buffer (PBS) (pH 7) for 10 s. The unreacted aldehyde functional groups on the IDE were then subsequently blocked by incubating with sodium borohydride (Na$_2$BH$_4$) to avoid any non-specific binding. Subsequently, 3 μl of E2 aptamer (10 μM) was incubated on apt/NH$_2$-GO/PPy/IDE for 15 min at room temperature. After incubation, the electrode rinses thoroughly with PBS to remove any abound E2 on the electrode surface. Each stage of the electrode modification process was monitored, and capacitance changes were quantified using impedance spectra data.

Analysis in real samples

Real water samples were collected from the Sungai Langat (Malaysia) throughout the application studies and filtered through a 0.45-μm pore membrane filter to eliminate the
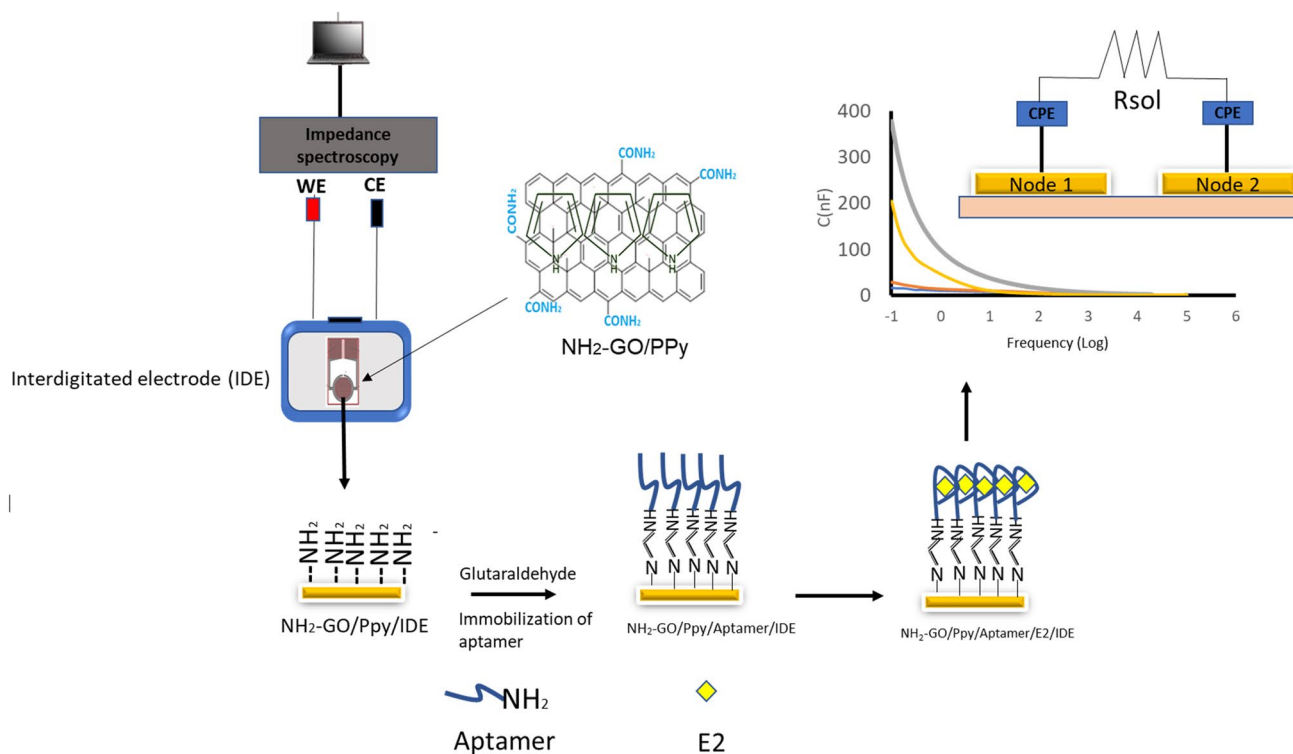

Fig. 1 The schematic stepwise procedure of aptasensor development for E2 detection

suspended particulate matter. The samples were spiked with E2 at concentrations of 1 ng/ml and 5 ng/ml, respectively. In addition, HPLC has been used to evaluate 17b-estradiol using real sample water with the condition as a previous study [32].

Results and discussion

Morphology characterization

The surface morphology and topography of NH_2-GO/PPy nanocomposite were observed using FESEM and AFM. From Fig. 2a, the texture of NH_2-GO/PPy has displayed a groove surface pattern and a rippling surface texture, suggesting the emergence of PPy with NH_2-GO. PPy was expected to be successfully blended with GO since graphene oxide is a universal nanofiller [20]. Subsequently, Fig. 2b
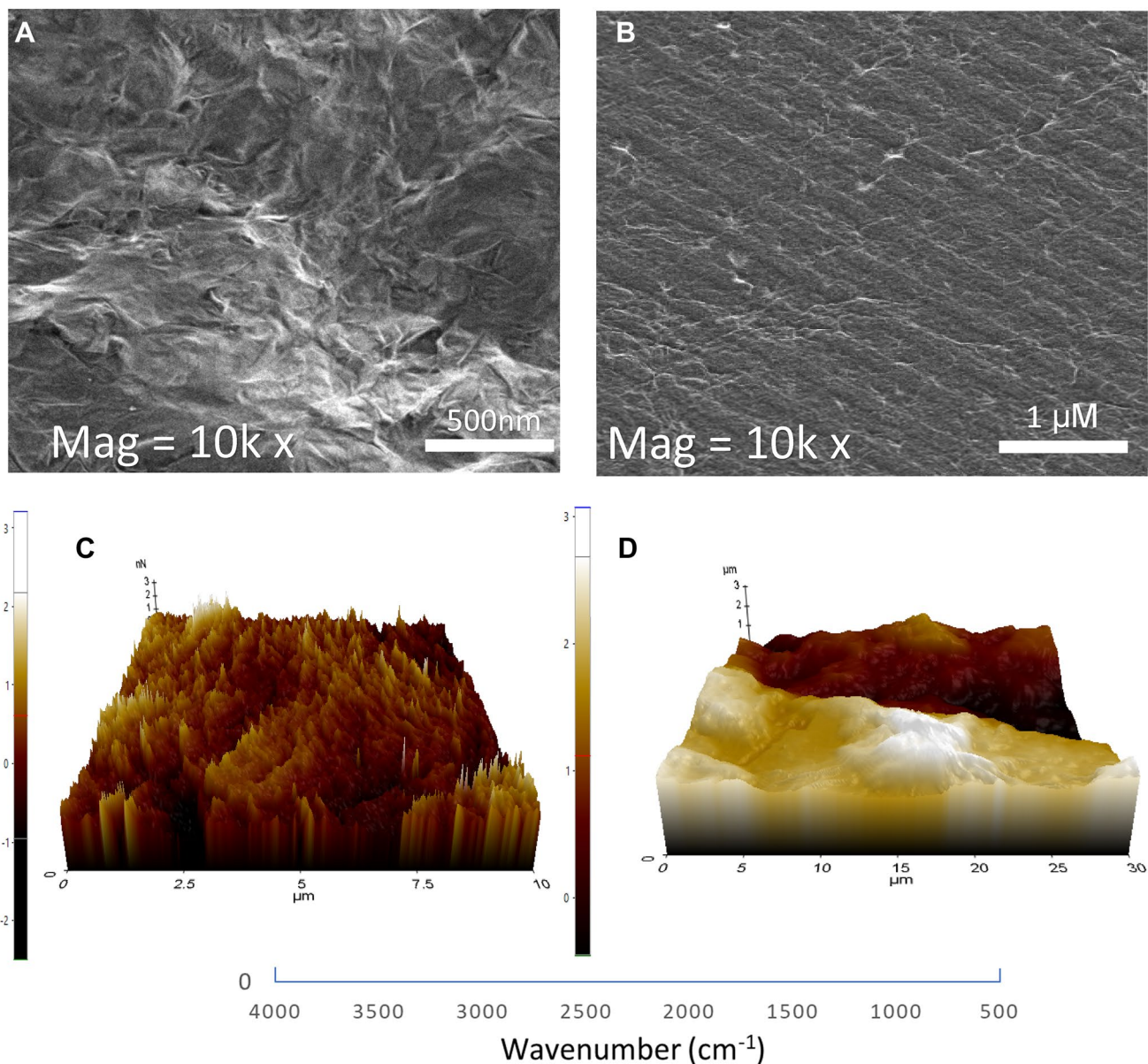

Fig. 2 FESEM images of (A) NH2-GO/PPy, (B) NH2-GO/PPy-modified IDE. AFM images of (C) NH2-GO-modified IDE, (D) NH2-GO/PPy-modified IDE

depicts the morphology of NH$_2$-GO/PPy deposition on IDE. We could observed the composite material evenly covered the entire surface of the IDE, indicating that the NH$_2$-GO/PPy deposition generated by moderate evaporation does not result in accumulation in a localized manner producing uniform distribution and efficient biomolecule immobilization.

Subsequently, NH$_2$-GO/PPy/IDE surface was examined by three-dimensional (3D) atomic force micrographs (AFM) to investigate the surface roughness and electrode thickness. Figure 2c shows the tapping mode AFM images of the deposited NH$_2$-GO/PPy on IDE with the lateral dimensions of the NH$_2$-GO/PPy flakes ranging from 1 to 10 μm. The average thickness of the sample was estimated to be 0.2 μm with a corresponding RMS roughness value of 40 nm. Previous studies showed that surface roughness is a critical factor which could influence the electrode's capacitive current. The findings demonstrate that the capacitance increases as the surface roughness increases [33].

Characterization by FTIR

Subsequent analysis was performed using Fourier transform infrared spectroscopy (FTIR) as shown in Fig. 3 which represents spectrum a) NH$_2$-GO, b) Pure PPy, and c) NH$_2$-GO/PPy, respectively. The characteristic absorption bands of amine groups, such as the N–H stretching vibration peak at 3431 cm^{-1}, the vibration and deformation peaks of C-N groups at 1417 cm^{-1}, and the C–O (alkoxy) stretching peak at 1051 cm^{-1}, are shown in NH$_2$-GO (Spectrum a) [36], while the synthesized PPy (Spectrum b) shows the weak

band at 2100 cm^{-1} is due to C-H stretching. Other peaks at 1505 and 1435 and 1000 cm^{-1} represent C-N, C-H plane deformation bonds, and C–C stretching which are also characteristic of the vibrations of pyrrole rings [37]. Moreover, NH$_2$-GO/PPy (spectrum c) showed PPy typical peaks present in the composites indicating successful polymerization of PPy, while a broad peak at 3281 cm^{-1} ascribed to the N–H stretching vibrations of the amine group suggesting GO reduction by EDA [38].

Optimization of the sensing conditions

Prior to conducting measurement, the effect of aptamer concentration and solution ionic strength has been conducted to examine the change in the modified IDE's capacitance. The results in Fig. 4a show the aptamer concentration was varied from 5 μM to 15 μM and was incubated with 1000 pM E2. This result indicated that 10 μM is near the initial signal saturation level for the capacitive aptamer-based biosensor. Therefore, 10 μM was used in all subsequent experiments. Subsequently, we verified the influence of the ionic force of the supporting electrolyte on the sensor response by varying the ionic strength of the electrolyte containing a NaCl concentration from 50 to 100 Mm according to a previous report pH since aptamer had the highest affinity for substrate at this pH [39]. Therefore, we opted pH 7.2 as pH for supporting electrolyte. As shown in Fig. 4b a drastic fall in capacitive changes was observed beyond 150 mM NaCl. This phenomenon could be due to the shielding of negative
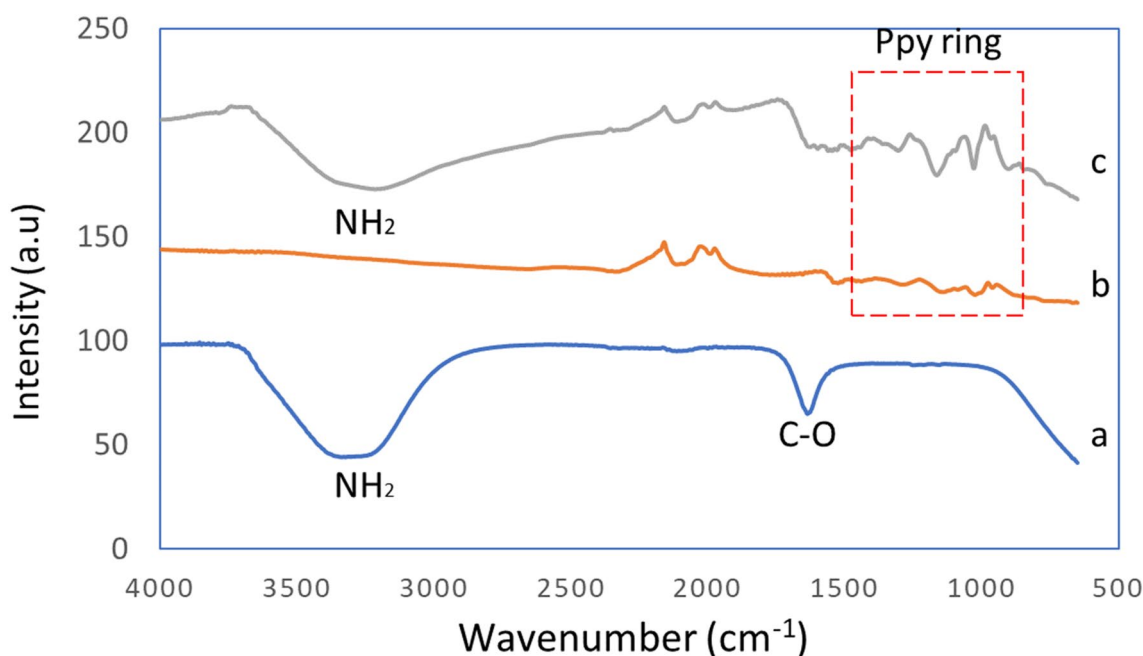

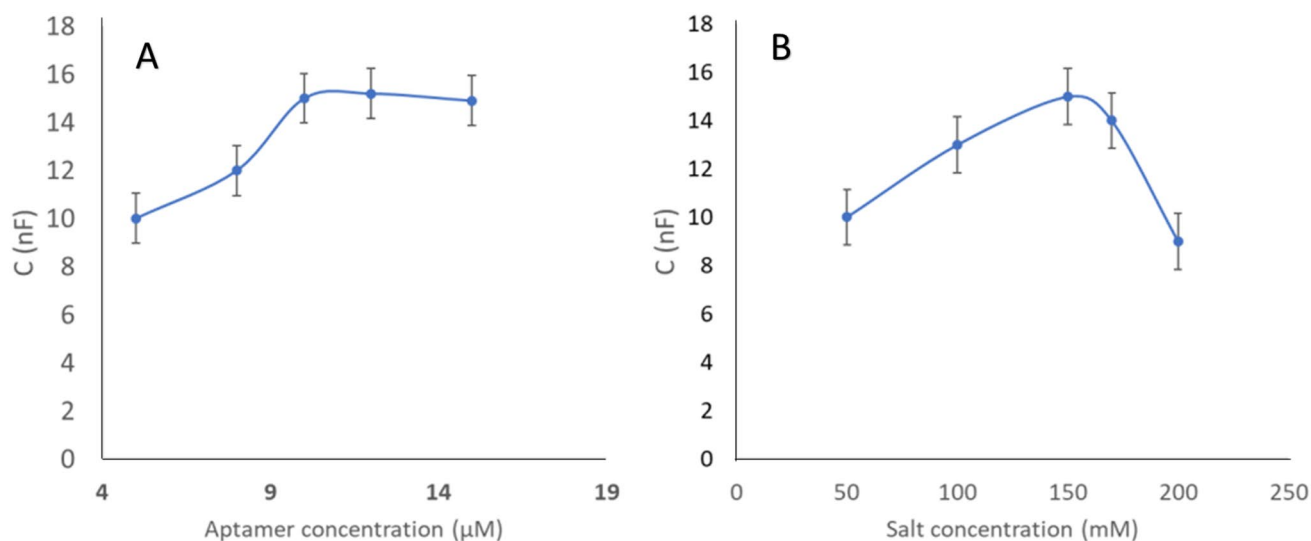**Fig. 3** **a** FTIR spectrum of PPy and **b** Gr/PPy

Fig. 4 **a** Effect of aptamer concentration. **b** Effect of ionic strength at various NaCl concentrations

charges at DNA aptamers and protein surfaces or changes in the binding site's conformation. [40]

Capacitive measurement via *electrochemical impedance*

In order to observe the capacitance variation of the modified IDE electrode, the obtained data from EIS were analyzed and fitted to equivalent circuits in the form of loops consisting of an imaginary constant phase element (CPE) in parallel with solution resistance, as illustrated in Fig. 5a. The capacitance determined based on this model was calculated using the equation $= 1/\omega Z''$ where ω is the angular frequency and Z'' the imaginary part of the impedance [41]. In Fig. 5b, the comparison of capacitance was extracted from the non-Faradic impedance measurement of gold IDE (Line a), PPy/IDE (Line b), and NH$_2$-GO/PPy/IDE (Line c) in the wide range of frequency between 0.1 Hz and 100 kHz. The calculated capacitance is inversely proportional to the log frequency, with the increment of capacitance at lower frequencies and becoming negligible at higher frequencies. According to Min et al. 2015, the total capacitance is considerably increased in the lower-frequency region due to the electrical double layer (EDL) caused by the formation of a space charge layer. At the higher-frequency region, the total capacitance is hugely affected by the geometric capacitance [42]. Based on this plot, the IDE with NH$_2$-GO/PPy exhibited capacitive was estimated to be 76 ± 3 nF at the frequency of 1 Hz which also the highest capacitance was recorded (line c), followed by PPy/IDE where its capacitance was 59 ± 2.5 nF (Line b) and bare gold IDE was about 48 ± 2 nF (line a), respectively. These results show that the synergetic combination between NH$_2$-GO and PPy has generated

the highest capacitance due to the π–π stacking between the NH$_2$-GO layers and the main chain of the aromatic PPy ring. Moreover, the higher surface area possessed by NH$_2$-GO/PPy allows the amount of charge accumulated on the NH$_2$-GO/PPy/IDE since the surface area of the electrode increases proportionally with capacitance [43].

Subsequently, the capacitance variation was recorded at various stages of electrode preparation during aptabiosensor development. As shown in Fig. 4c, NH$_2$-GO/PPy/IDE exhibited the highest capacitance (Line a) in its steady state. However, a further substantial decrease in capacitance response approximately 49% was found when NH$_2$-GO/PPy/IDE was crosslinked with glutaraldehyde (Line b). Then, a further decrease of about 38% occurred following aptamer immobilization (Line c) which could be due to insulating effect of the crosslinker and aptamer. This result can also be related to the successful self-assembly of aptamer on the modified electrode. The capacitance continued to drop after 17β-estradiol (E2) was introduced onto the electrode, where the binding was supposed to occur (Line d). We presume that this change in capacitance is not due to an insulating effect; however, it is due to partial change of the aptamer conformation upon binding to E2, which produce more charge accumulation on the electrode surface and thus decrease the capacitance.

Aptasensor performance

Investigation of the developed aptasensor on its sensitivity was further carried out by varying concentrations of E2. As depicted in Fig. 6a, we plotted the graph for capacitance against E2 concentration from the non-Faradic EIS resulting in the decreasing of capacitance with the increasing E2
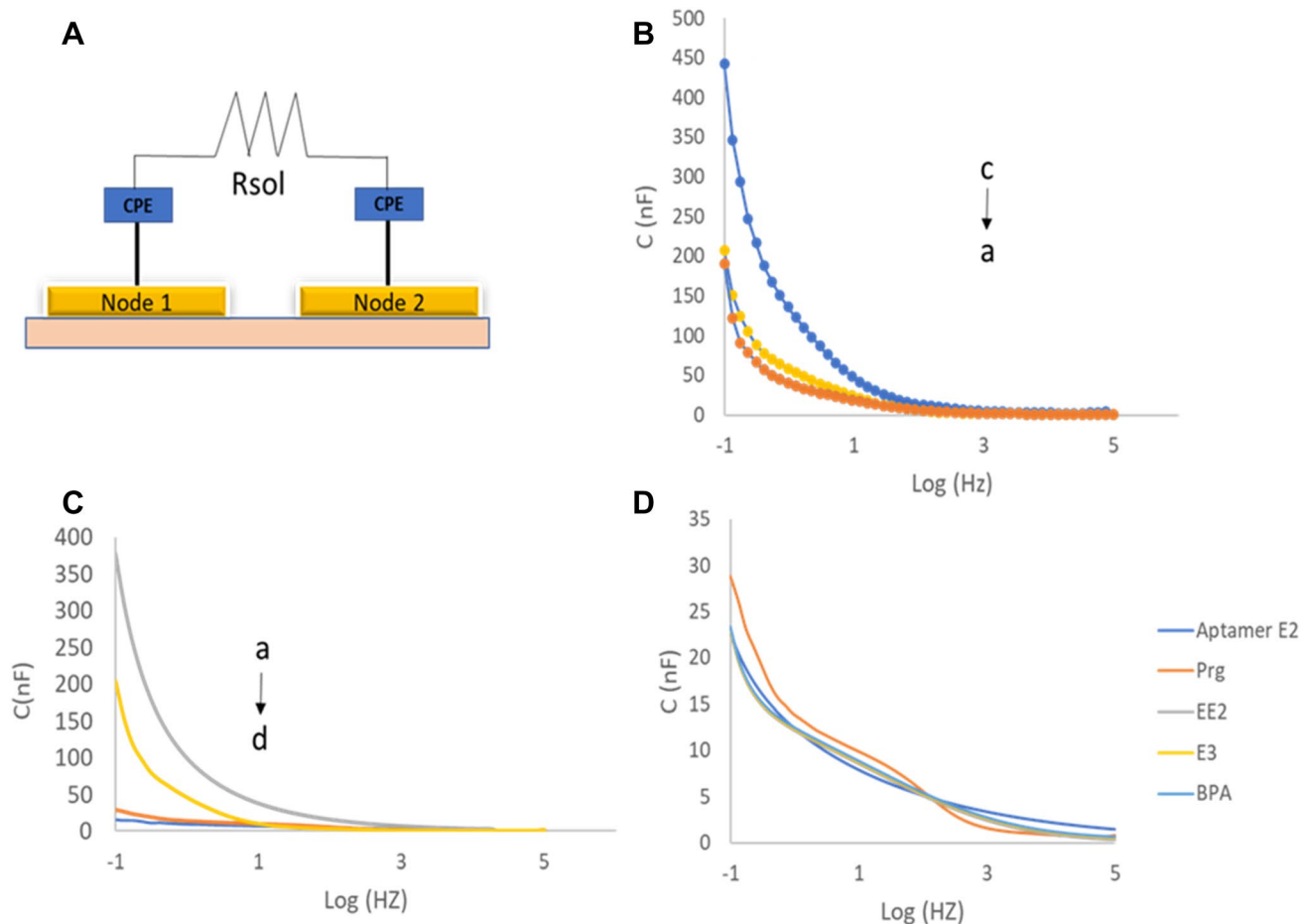
Fig. 5 The equivalent circuit model for fitting the impedimetric experimental data. (B) Capacitance variation of different electrode modifications against log frequency of **a** NH2-GO-PPy/IDE, **b** PPy/IDE, **c** IDE (Hz). (C) Capacitance change from various modifica-tion stages plot against log frequency (Hz) of **a** NH2-GO-PPy/IDE, **b** NH2-GO-PPy/IDE/Glu, **c** Apt/Glu/NH2-GO/PPy/IDE, **d** E2/Apt/Glu/NH2-GO/PPy/IDE

concentrations in the range of 1000 to 1 pM. This decrease was observed due to applied frequencies ranging from 0.1 to 100 kHz, which demonstrated successful E2 capture by aptamer on the surface of modified IDE. Moreover, the capacitance shift can be seen where capacitance values at 1 Hz elicit the most significant capacitive effect as displayed in the bode plot (Inset). Based on this evaluation, capacitance values at 1 Hz were then utilized to plot the calibration curve for capacitance changes against E2 concentrations in PBS for the calculation of the LOD by linear regression. The capacitance changes (ΔC) were calculated from the data obtained using the equation:

$$\frac{c - c_0}{c_0} \times 100 \qquad (1)$$

where C is the actual capacitance after aptamer binding with E2 at a particular concentration and C_0 is the capacitance before binding. Thus, the calibration plot shown in Fig. 6b

can be represented by the equation $C = 1.28x + 17.5$ ($R2 = 0.994$) with a detection limit of 0.13 pM using the equation of 3S/b, where S is the standard deviation of the blank and b is the slope of the straight line. The obtained standard deviations ranged from 1% to 4%, indicating that the established E2 aptasensor was highly reproducible and provided fast, label-free, and reliable potentials for on-site use. However, several research studies have reported sensor-based aptamers of different lengths with increased LOD [39]. However, they are unsuitable for on-site aptasensor use due to additional electrode requirements and chemical usage.

Specificity and stability of the developed aptasensor

Several control experiments were carried out to demonstrate the influences of non-specific adsorption, sensor specificity, and aptamer selectivity. Therefore, three chemicals from similar classes that coexist with E2 in water sources
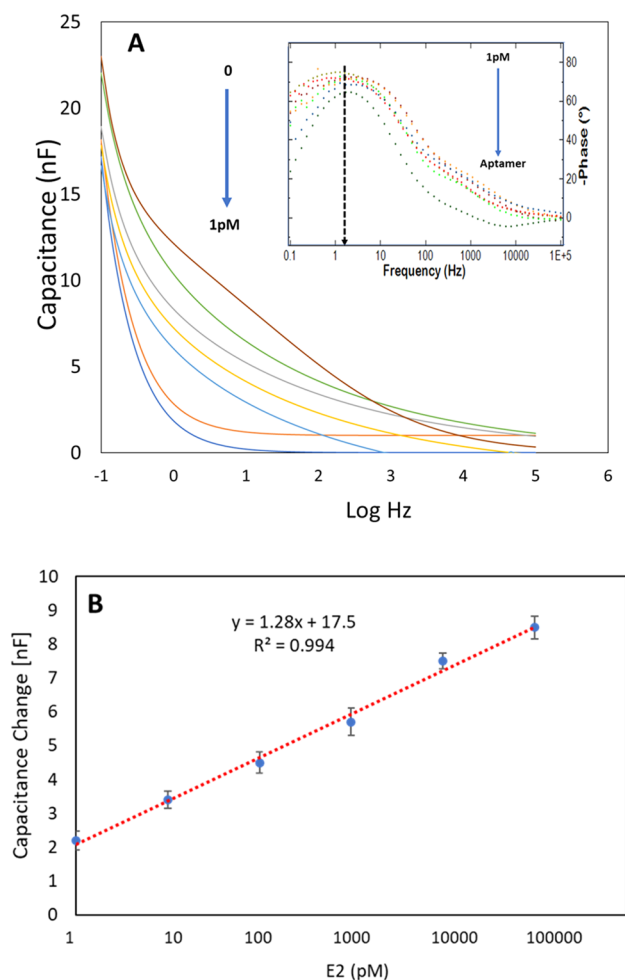
Fig. 6 **a** Aptasensor response to different concentrations of E2; **b** linear calibration curve of capacitance changes with various E2 concentrations

were chosen, namely (BPA), (E3), and (EE2), respectively, to evaluate the sensor's ability to interfere with the target 17-estradiol. This chemical was exposed to the aptasensor containing 1×10^{-9} M of E2, and its capacitance was determined using previously described procedures. As illustrated in Fig. 7, the capacitance difference (C) between pre- and post-incubation with 5.0 nM E2 demonstrated less than 15% of the changes, indicating that no significant interference effect was induced by species other than E2. This can also be attributed to the fact that E2 is not captured on the sensing

surface because the interference compound appears to lack an E2 recognition site. In addition, aptasensor stability was stored at 4° C for 28 days, as demonstrated in Fig. 7b. As can be seen, the final value retained 91.7% of its initial value and dropped at the weeks of four, indicating that the developed aptasensor has excellent storage stability as shown in Table 1.

Analysis of spiked E2 in river water

To demonstrate the potential application of the developed aptasensor, a sample of river water was collected and subsequently spiked with E2. As shown in Table 2, the percentage recovery of E2 was calculated by spiking a known concentration of E2 (20 and 25 ng/ml) to determine the accuracy of the procedure being developed. The calculated recovery is to be 99.3% and 103.0% ($n=3$), respectively, suggesting the recovery was good accuracy for determining E2 in real water samples. Subsequently, the developed biosensor was validated by comparing the results to those obtained using HPLC. As a result, two small peaks were detected at 3.8 and 5.9 min that could be related to E2 in the water matrix (Fig. 8S). Moreover, the t test shows there was no significant difference using aptasensor detection between the HPLC and developed methods at a 95% confidence level, showing that the proposed sensor can be used for the determination of E2 in water samples.

Conclusion

In this study, graphene oxide polypyrrole matrix (NH_2-GO/PPy) was synthesized as a supporting matrix and used as a non-Faradic capacitive biosensor aptamer-based strategy to monitor 17-estradiol (E2). Moreover, the developed aptasensor demonstrated excellent selectivity when confronted with a similar structure interferences compound (EE2, BPA, E3) and exhibited an excellent sensitivity of 0.13 pM. Furthermore, measurement was taken without redox probe allowing on-site monitoring to implement low-cost and rapid biosensors. The practicability of the proposed aptasensor was verified by HPLC with the satisfied recoveries of the spiked E2 in the river water sample. Moreover, the fabrication method is simple and could be used to detect other estrogen compounds in natural water samples paving the way to a new generation of alternative low-cost and rapid biosensors.

Fig. 7 a The specificity of the aptasensor was studied with the four groups of interferences which frequently detected in the water. Several EDCs such as estriol (E3), progesterone (PRG), and bisphenol A (BPA) were tested, respectively
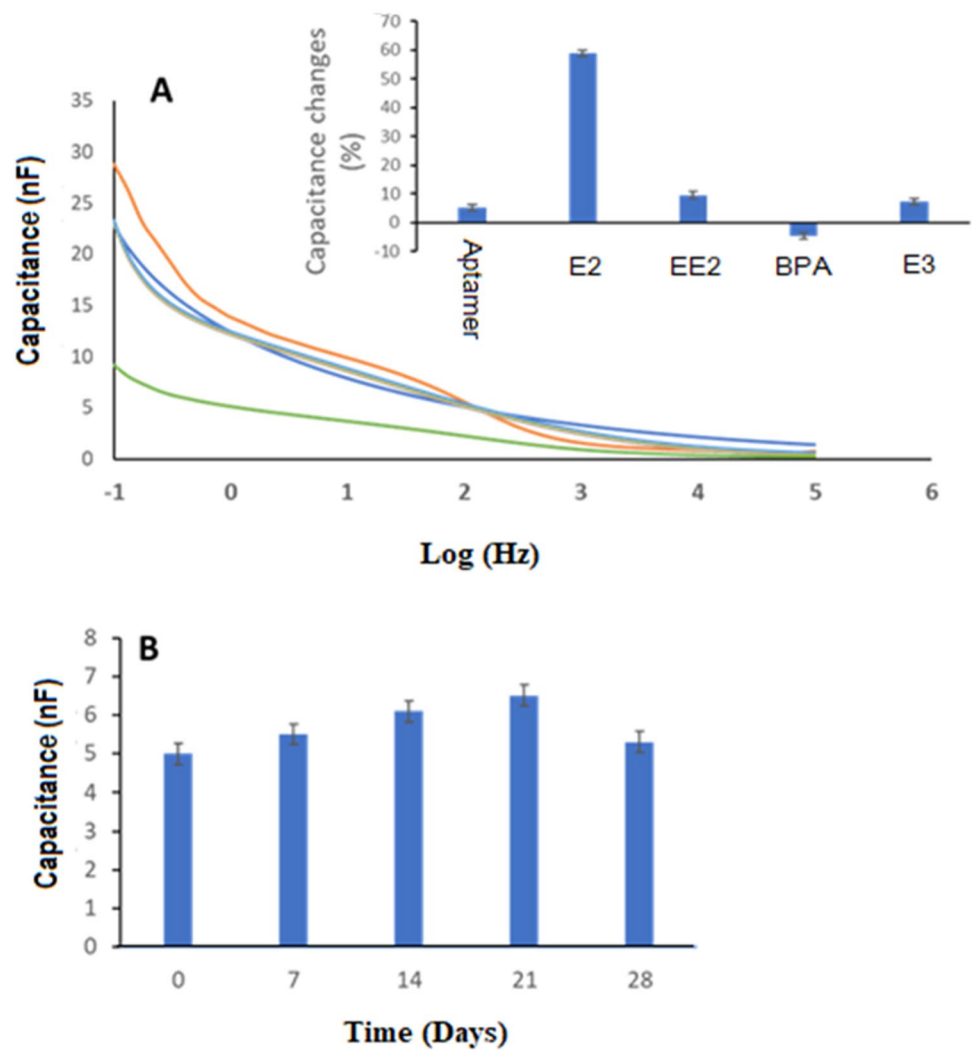

Table 1 Comparison of limit of detection (LOD) for some developed label-free aptasensor for E2 determination

Electrode	Method detection	Linear range	LOD	References
Gold electrodes	EIS	1×10^{-8}–1×10^{-11} M	2.0 pM	[43]
pNIPAm	Reflectance spectroscopy	0.9–200 pg/mL	3.2 pM	[44]
(NiHCF NPs)/AuNPs	DPV	1–1000 pM	0.8 pM	[45]
AuNP-Thi-CNTs	Ratiometric	12 pM to 60 nM	1.5 pM	[20]
CDs/SPCE	EIS	1×10^{7}–1×10^{12} M	0.5 pM	[46]
NH_2-GO/Ppy/IDE	EIS	1×10^{-8}–1×10^{-12}	0.13 pM	This work

Poly(N-isopropylacrylamide-microgel(pNIPAm); nickel hexacyanoferrate nanoparticles (NiHCF NPs)/gold nanoparticle (NiHCF NPs)/AuNPs; gold nanoparticles-thionine-multiwalled carbon nanotubes AuNP-Thi-CNTs; carbon dots/screen-printed electrode (CDs/SPCE)

Table 2 Detection of the real water samples with E2 at different concentrations as comparison with HPLC methods

Water sample	Added (ng/ml)	The developed method (ng/ml)	Recovery (%)	HPLC method (ng/ml)	Recovery (%)	t Test
River Water	20	20.6 ± 0.12	103.2	24.3 ± 0.01	97.2	0.01
	25	25.2 ± 0.63	99.3	21.4 ± 0.06	107	0.03
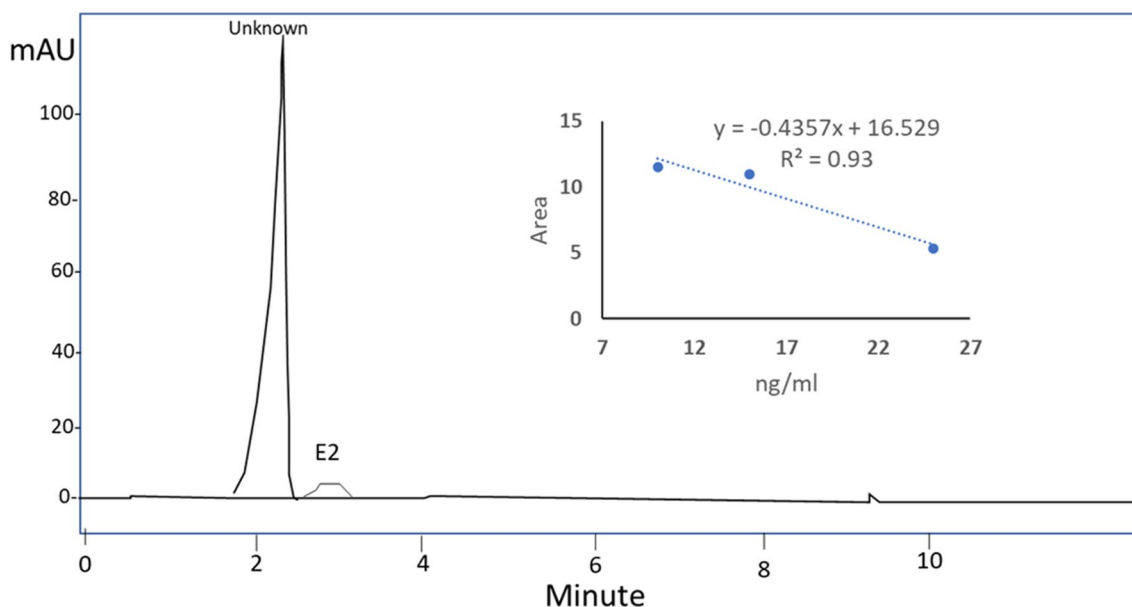
Fig. 8 The E2 determination in real water samples performed using HPLC

Declarations

Conflict of interest The authors declare no competing financial interest.

References

1. A. Gonsioroski, V.E. Mourikes, Flaws JA MDPI Int. J. Mol. Sci. **21**, 1929 (2020)
2. M. Kumar, D.K. Sarma, S. Shubham, M. Kumawat, V. Verma, A. Prakash, R. Tiwari, Front. Public Health **8**, 553850 (2020)
3. S.Y. Wee, A.Z. Aris, F.M. Yusoff, S.M. Praveena, Sci. Rep. **10**, 1 (2020)
4. W.J. Backe, Environ. Sci. Technol. **49**, 24 (2015)
5. M. Wooding, E.R. Rohwer, Y. Naudé. J. Chromatogr. A 1496 (2017)
6. C.I. Justino, A.C. Duarte, T.A. Rocha-Santos, Sensors **17**, 2918 (2017)
7. T. Chalklen, Q. Jing, S. Kar-Narayan, Sensors (Basel). **20**, 19 (2020)
8. H.L.L. Yu, A. Maslova, I. Hsing, ChemElectroChem **4**, 4 (2017)
9. K. Spychalska, D. Zajac, J. Cabaj, RSC Adv. **10**, 9079–9087 (2020)
10. D. Futra, Y. Heng, M.Z. Jaapar, A. Ulianas, K. Saeedfar, T.L. Ling, Anal. Methods **8**, 1381 (2016)
11. R.A. Olowu, O. Arotiba, S.N. Mailu, T.T. Waryo, P. Baker, Iwuoha E Sensors (Basel). **10**, 9872 (2010)
12. H. Pu, Z. Huang, D.W. Sun, X. Xie, W. Zhou, Water Air Soil Pollut. **230**, 6 (2019)
13. H. Huang, S. Shi, X. Gao, R. Gao, Y. Zhu, X. Wu, T. Yao, Biosens. Bioelectron. **79**, 198 (2016)
14. J. Zhou, J. Rossi, Nat. Rev. Drug Discov., vol. **16**(3) (2017)
15. H. Yoo, H. Jo, S.S. Oh, Mater. Adv **1**, 2663 (2020)
16. B. Hock, M. Seifert, K. Kramer, Biosens. Bioelectron. **17**, 239 (2002)
17. A. Kirchhain, A. Bonini, F. Vivaldi, N. Poma, and F. Di Francesco Trends Anal. Chem. **133**, 116073 (2020)
18. I. A. Mattioli, M. Baccarin, P. Cervini, and É. T. G. Cavalheiro, J. Electroanal. Chem., 835, (2019)
19. L. Zamfir, M. Puiu, C. Bala, Sensors **20**, 6443 (2020)
20. S.K. Arya, P. Zhurauski, P. Jolly, M.R. Batistuti, M. Mulato, P. Estrela, Biosens. Bioelectron. **102**, 106 (2018)
21. Z.G. Namhil et al., Phys. Chem. Chem. Phys. **21**, 681 (2019)
22. M. Acuautla, S. Bernardini, L. Gallais, T. Fiorido, L. Patout, M. Bendahan, Sensors Actuat. B. Chem. **203**, 602 (2014)
23. Y. Wu, W. Hong, T. Akiyama, S. Gautsch, IOP Sci. **24**, 235302 (2013)
24. K. Chou, C. Lee, Adv. Mater. Sci. Eng. **514508**, 1 (2014)
25. J.L. Hammond, M.C. Rosamond, S. Sivaraya, F. Marken, P. Estrela, Sensors **16**, 2128 (2016)
26. G.V. Soraya, Sci. Rep. **9**, 1 (2019)
27. G. Luka, E. Samiei, S. Dehghani, T. Johnson, H. Najjaran, M. Hoorfar, Sensors **19**, 258 (2019)
28. M. Sypabekova, K. Dukenbayev, A. Tsepke, A. Akisheva, N. Oralbayev, D. Kanayeva, Sci. Rep. **9**, 1 (2019)
29. A. Qureshi, Y. Gurbuz, S. Kallempudi, J.H. Niazi, Phys. Chem. Chem. Phys. **12**, 9176 (2010)
30. E. Kostal, S. Kasemann, C. Dincer, S. Partel, Multidiscip. Digit. Publ. Inst. Proc. **2**(13), 899 (2018)
31. Singh, Ravindra P. International journal of electrochemistry 2011 (2011).
32. A.N. Banerjee, Interface Focus **8**, 20170056 (2018)
33. O. Movil, C. Schadeck, J.A. Staser, J. Electroanal. Chem. **755**, 127 (2015)
34. R. Khan, Y. Nishita, J. Mater. Chem. A **8**, 13718 (2020)
35. M.J. Dunlop, R. Bissessur, J. Mater. Sci. **55**, 6721 (2020)

36. J. Zhao, Wu. Jinping, B. Li, Du. Weimin, Q. Huang, M. Zheng, H. Xue, H. Pang, Prog. Nat. Sci. Mater. Int. **26**, 237 (2016)

37. T.C. Girija, M.V. Sangaranarayanan, J. Power. Sources **159**, 1519 (2006)

38. Y. Xu, J. Wang, W. Sun, S. Wang, J. Power. Sources **159**, 370 (2006)

39. Y. Kim Seok, H. Sup Jung, T. Matsuura, H. Yeon Lee, T. Kawai, and M. Bock, Biosens. Bioelectron., **22**, 2525 (2007)

40. S. Pourbeyram, P. Kheyri, Synth. Met. **238**, 22 (2018)

41. F.C. Moraes, B. Rossi, M.C. Donatoni, K.T. De Oliveira, E.C. Pereira, Anal. Chim. Acta **881**, 37–43 (2015)

42. H. Chang, C. Chang, Y. Tsai, and C. Shiun Liao, Carbon N. Y., **50**, 2331 (2012)

43. H. Zhang, X. Liu, H. Li, N. Chen, Y. Fu, Key Eng. Mater. **565**, 1461 (2013)

44. J. Ederer, P. Janoš, P. Ecorchard, J. Tolasz, V. Štengl, H. Beneš, M. Perchacz, O. Pop-Georgievski, RSC Adv. **7**, 12464 (2017)

45. C. Zhu, J. Zhai, D. Wen, and S. Dong, J. Mater. Chem., **22**, 6300 (2012)

46. Z. Lin, L. Chen, G. Zhang, Q. Liu, B. Qiu, Z. Cai, G. Chen, Analyst **137**, 819 (2012)

47. Y. Jiang, M.G. Colazo, M.J. Serpe, Anal. Bioanal. Chem. **410**, 4397 (2018)

48. L. Fan, G. Zhao, H. Shi, M. Liu, Biosens. Bioelectron. **68**, 303 (2015)

49. X. Liu, K. Deng, Microchim. Acta **186**, 347 (2019)

50. M. Hazani, M. Zaid, J. Abdullah, N. Rozi, S.A. Hanifah, Nanomaterials **10**, 1346 (2020)